catalysts

MDPI

Article

Highly Tuning of Sunlight-Photocatalytic Properties of SnO_2 Nanocatalysts: Function of Gd/Fe Dopants

Ghayah M. Alsulaim [1,*] and Shada A. Alsharif [2]

[1] Department of Chemistry, Faculty of Science, King Faisal University, Al Ahsa 31982, Saudi Arabia
[2] University College of Umluj, Tabuk University, Tabuk 71491, Saudi Arabia; shalsharif@ut.edu.sa
* Correspondence: galsaleem@kfu.edu.sa or g.m.alsulaim@gmail.com

Abstract: Gd/Fe-SnO_2 nanopowders as novel photocatalysts for the active removal of Rose Bengal dye and methyl parathion pesticide were synthesized with a low-cost coprecipitation route. The X-ray diffraction analysis of SnO_2, $Sn_{0.96}Gd_{0.02}Fe_{0.02}O_2$ and $Sn_{0.94}Gd_{0.02}Fe_{0.04}O_2$ nanopowders proved the formation of a tetragonal phase of tin oxide with average crystallite sizes in the range of 13–18 nm. The Fourier transform infrared (FTIR) spectra of all samples displayed the characteristic absorption bands of SnO_2. The nanopowder of the pure SnO_2 sample, as seen in its transmission electron microscope (TEM) image, contains spherical-like particles of variable sizes. The TEM images of the $Sn_{0.96}Gd_{0.02}Fe_{0.02}O_2$ and $Sn_{0.94}Gd_{0.02}Fe_{0.04}O_2$ powders revealed the synthesis of fine spherical nanoparticles. Based on the TEM images, the average particle size of the pure, (Gd, 2 wt% Fe) and (Gd, 4 wt% Fe) codoped SnO_2 nanopowders was estimated to be 14, 10 and 12 nm, respectively. After the addition of (Gd, 2 wt% Fe) and (Gd, 4 wt% Fe) to the SnO_2 structure, the band gap energy of SnO_2 was reduced from 3.4 eV to 2.88 and 2.82 eV, respectively. Significantly, the $Sn_{0.96}Gd_{0.02}Fe_{0.02}O_2$ nanocatalyst exhibited a high removal efficiency of 98 and 96% for Rose Bengal dye and methyl parathion pesticide after activation by sunlight for 35 and 48 min, respectively. Furthermore, this catalyst has shown perfect mineralization as well as high stability properties for the treatment of Rose Bengal dye and methyl parathion pesticide. These results suggest the suitability of the $Sn_{0.96}Gd_{0.02}Fe_{0.02}O_2$ nanocatalyst for the treatment of agriculture and industrial effluent under sunlight light energy.

Keywords: agriculture and industrial wastewater; SnO_2 semiconductor; codoping; solar energy; photocatalysis

Citation: Alsulaim, G.M.; Alsharif, S.A. Highly Tuning of Sunlight-Photocatalytic Properties of SnO_2 Nanocatalysts: Function of Gd/Fe Dopants. *Catalysts* **2024**, *14*, 347. https://doi.org/10.3390/catal14060347

Academic Editor: Ewa Kowalska

Received: 8 May 2024
Revised: 23 May 2024
Accepted: 25 May 2024
Published: 28 May 2024

1. Introduction

Many organic pesticides are used to eliminate harmful insects and pests in order to increase the agricultural production of various grains and fruits [1,2]. The reported data indicated that nearly 3 million tons of different pesticides (insecticides, herbicides, algaecides, fungicides, etc.) are used every year [3]. To increase the quality of clothing, leather and paper products, many colored organic dyes are used for this propose [4,5]. Annually, the worldwide used quantities of colored organic compounds reach to two million tons [6]. A large proportion of agriculture pesticides and industrial dyes are drained into water systems as wastewater every day without any pre-treatment [7,8]. Despite the benefits of these organic compounds, they have many harmful effects that cause many health problems for humans, animals, plants and aquatic systems [9,10]. Beside the high toxicity and hazardous effects of these organic materials, they have high stability and do not easily decompose into the environment [11,12]. Removing these pollutants (dyes, pesticides) from the surrounding environment is extremely important for all living creatures [13,14]. Scientists and researchers have studied many methods such as adsorption [15], photocatalysis [16], coagulation–flocculation [17] and membrane filtration or ultra-filtration [18] to effectively deal with these pollutants. Solar energy-based photocatalysis emerged as

a sustainable method with perfect performance to completely eliminate the toxic and harmful organic materials from wastewater [19,20]. One of the essential requirements of the sunlight-based photocatalysis strategy is the design of full-spectrum or broad visible light catalysts to make the most of solar energy [21,22]. Many studies investigated the modifications of semiconductor metal oxides such as ZnO [23], TiO_2 [24], WO_3 [25], In_2O_3 [26] and SnO_2 [27] to function as efficient visible light photocatalysts for wastewater treatment. Nanostructured tin oxide (SnO_2) is one of the important n-type semiconductor metal oxides with a large band gap energy of 3.6 eV [28]. SnO_2 has interesting optical, electrical and gas sensing properties with wide promising applications in gas sensors [29], solar cells [30] and photocatalysis [31]. Mezyen et al. [27] investigated the photocatalytic degradation of SnO_2:Dy thin films for methylene blue dye under sunlight irradiation. They found that SnO_2 containing 5% Dy thin film revealed a 90.99% degradation efficiency after 3 h. Moreover, a 5% mole copper-doped SnO_2 nanoparticles synthesized through a co-precipitation approach exhibited 100% degradation efficiency for Rhodamine B dye in 60 min under UV–Visible light irradiation [32]. Baig et al. [33] illustrated that 4% mole Fe-doped SnO_2 nanoparticles prepared through the microwave-aided co-precipitation method have a photo-degradation efficiency of 87.2% for methyl orange in 200 min under visible light irradiation. In recent years, the integrations and combinations of the different dopants were used to advance the photocatalytic activity of many metal oxides [34,35]. After reviewing the published results, the impact of Gd/Fe ions as a co-dopants mixture on the optical response and photocatalytic activity of nanosized SnO_2 powders for the removal of pesticides and dyes has rarely been studied. In this research, SnO_2, $Sn_{0.96}Gd_{0.02}Fe_{0.02}O_2$ and $Sn_{0.94}Gd_{0.02}Fe_{0.04}O_2$ nanopowders were prepared by precipitation. The photocatalytic activity of these nanopowders for the removal of Rose Bengal dye and methyl parathion pesticide was measured under sunlight energy. The physical and chemical properties of the prepared nanopowders were characterized by using different techniques including XRD, FTIR, TEM and diffuse reflectance techniques. The photocatalytic results proved that the addition of (2 wt% Gd + 2 wt% Fe) ions strongly activated the photodegradation performance of SnO_2 nanopowders, with nearly 100% removal efficiency for the tested dye and pesticide over 35–48 min.

2. Results and Discussion

2.1. X-ray Diffraction (XRD)

The crystal structure of the prepared SnO_2, $Sn_{0.96}Gd_{0.02}Fe_{0.02}O_2$ and $Sn_{0.94}Gd_{0.02}Fe_{0.04}O_2$ nanopowders was determined by XRD analysis, as shown in Figure 1. The XRD patterns of the undoped and codoped samples showed definite and intense diffraction peaks exactly related to (110), (101), (200), (211), (220), (002), (310), (112), (301), (202) and (321) planes of the tin oxide (SnO_2) structure with tetragonal phase, in agreement with the Joint Committee on Powder Diffraction Standards (JCPDS, ≠PDF no. 41-1445). Moreover, these patterns are free from any contaminated peaks, proving the purity of the samples. The substitution of Gd and Fe ions for Sn^{4+} positions inside the SnO_2 structure was studied by identifying the change in position of the 2-theta angle of the main (100) crystallographic plane as well as by measuring the variation in the lattice parameter of all samples. As shown in Figure 2a, the magnified pattern of the (100) crystallographic plane displays that the additives of Gd/Fe ions move the position of the (100) plane toward a low 2-theta angle, suggesting the expansion of the SnO_2 lattice. The measured lattice dimensions of pure and Gd/Fe samples confirmed that the lattice constants "a" and "c" of pure tetragonal SnO_2 were increased due to the additions of Gd/Fe ions, as seen in Figure 2b,c. The ionic radius of Sn^{4+} is 0.69 Å, while the ionic radii of the Gd^{3+} ion is 0.938 Å, of Fe^{2+} is 0.61 Å and of Fe^{3+} is 0.55 Å. The expansion of the lattice constant can be mainly linked to the effect of Gd^{3+} (0.938 Å) ions owing to the sensible difference in ionic radius with Sn^{4+} ions, which overcome on the effect of Fe. These results verify the replacement of Gd^{3+} (0.938 Å) and Fe^{2+} (0.61 Å)/Fe^{3+} (0.55 Å) for Sn^{4+} sites inside the SnO_2 lattice. The crystallite size of

the prepared SnO_2, $Sn_{0.96}Gd_{0.02}Fe_{0.02}O_2$ and $Sn_{0.94}Gd_{0.02}Fe_{0.04}O_2$ nanopowders was found using the well-known method based on the Scherer Equation (1) [36]:

$$D = \frac{0.9\lambda}{\beta cos\theta} \quad (1)$$

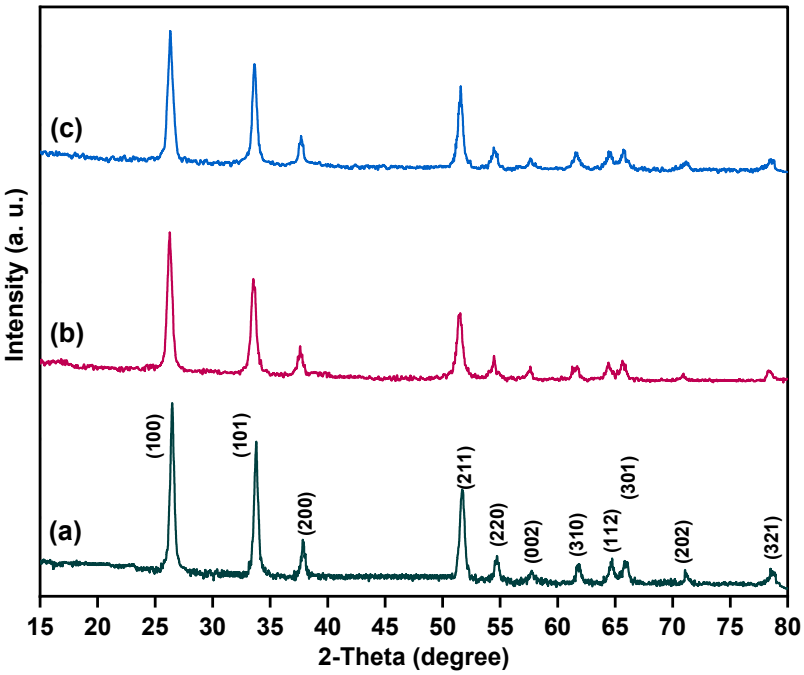

Figure 1. Patterns of X-ray diffraction of (**a**) pure SnO_2, (**b**) $Sn_{0.96}Gd_{0.02}Fe_{0.02}O_2$ and (**c**) $Sn_{0.94}Gd_{0.02}Fe_{0.04}O_2$ nanopowders.

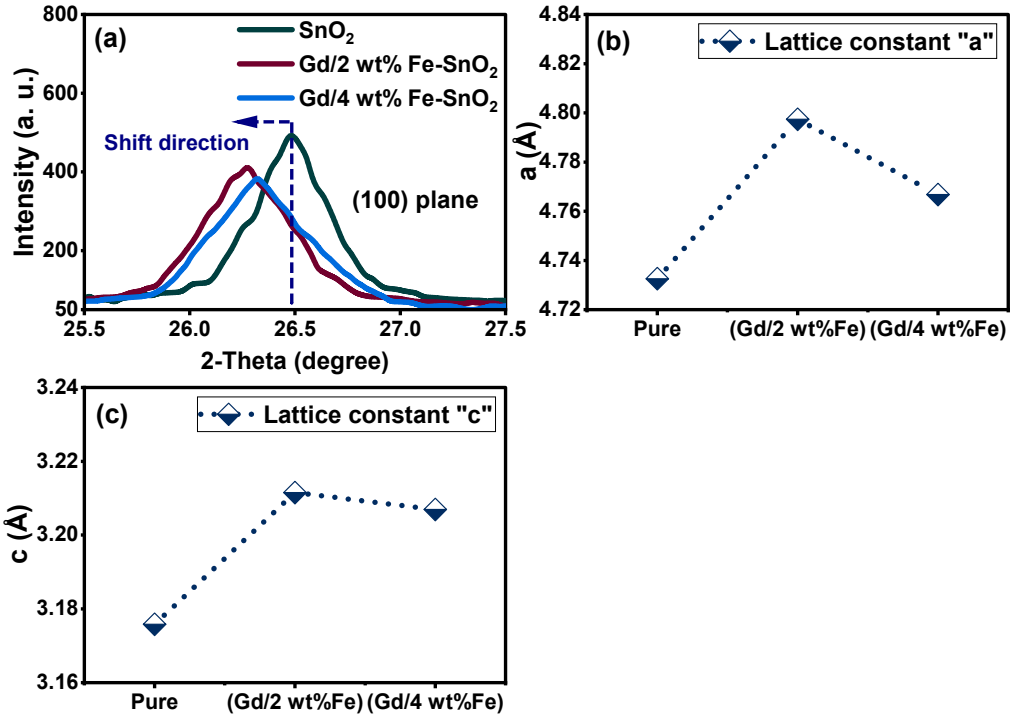

Figure 2. Effect of Gd/Fe ions codoping on (**a**) 2-theta position of (100) plane of SnO_2, (**b**) lattice constant "a" and (**c**) lattice constant "c" of tetragonal SnO_2.

The λ is the wavelength of the X-ray diffraction (1.5406 Å), θ is the angle of the XRD peaks; β is the width at half height for the five most intense peaks. The recorded crystalline sizes of SnO_2, $Sn_{0.96}Gd_{0.02}Fe_{0.02}O_2$ and $Sn_{0.94}Gd_{0.02}Fe_{0.04}O_2$ nanopowders are 18, 14 and 13 nm, which are in agreement with the subsequent results from the transmission electron microscope (TEM) images.

2.2. FTIR Spectra

Figure 3 depicts the Fourier transform infrared (FTIR) spectra of pure SnO_2, $Sn_{0.96}Gd_{0.02}Fe_{0.02}O_2$ and $Sn_{0.94}Gd_{0.02}Fe_{0.04}O_2$ nanopowders within wavenumber range from 400 to 4000 cm^{-1}. The FTIR curve of pure SnO_2 nanopowders shows different absorption bands located at ~3442, 1624, 617 and 529 cm^{-1}, which were linked to stretching vibrations of the OH group, bending vibrations of the OH group, O-Sn-O and finally Sn-O vibrations, respectively. The vibrations of OH groups were attributed to the adsorbed H_2O and OH groups trapped in the SnO_2 nanoparticles [37,38]. The FTIR curves of $Sn_{0.96}Gd_{0.02}Fe_{0.02}O_2$ and $Sn_{0.94}Gd_{0.02}Fe_{0.04}O_2$ nanopowders have shown similar spectra to that obtained for the pure SnO_2 sample. The center of the two characteristic absorption bands of O-Sn-O and Sn-O vibrations was found at 607 and 521 cm^{-1} for the $Sn_{0.96}Gd_{0.02}Fe_{0.02}O_2$ sample while the $Sn_{0.94}Gd_{0.02}Fe_{0.04}O_2$ sample exhibits the two characteristic absorption bands at 607 and 519 cm^{-1}. The slight changes in the wavenumber position of the two characteristics absorption bands suggest the substitution of Gd and Fe ions for Sn^{4+} sites in the SnO_2 structure. The results of the FTIR are in agreement with the X-ray diffraction study, which supports the purity of the compositions and the effect of Gd/Fe dopants on the lattice structure.

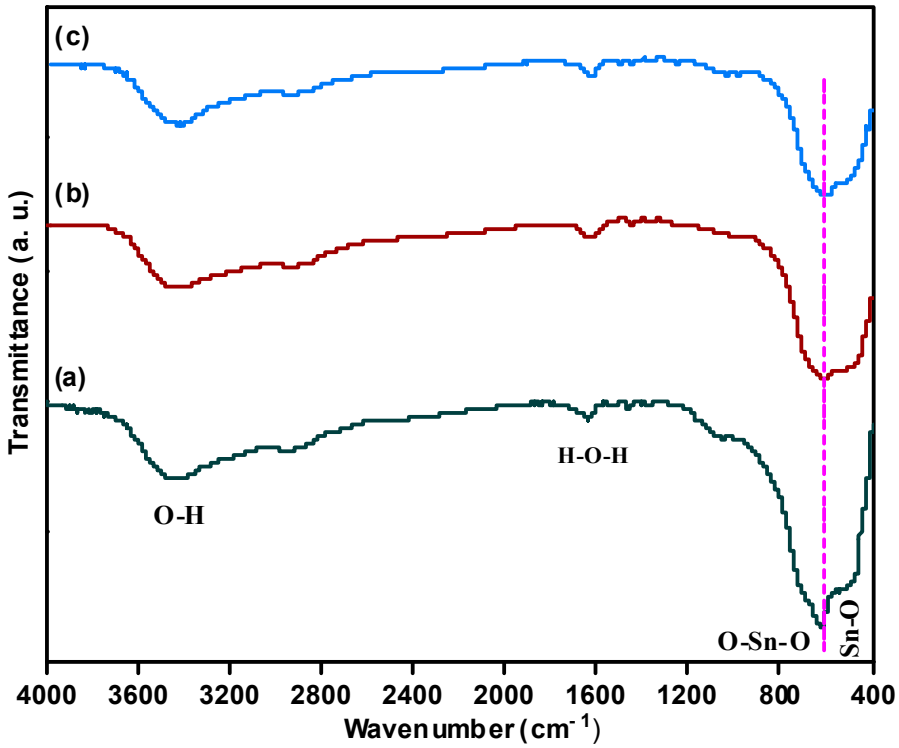

Figure 3. FTIR curve of (**a**) pure SnO_2, (**b**) $Sn_{0.96}Gd_{0.02}Fe_{0.02}O_2$ and (**c**) $Sn_{0.94}Gd_{0.02}Fe_{0.04}O_2$ nanopowders.

2.3. Transmission Electron Microscope (TEM)

The particles size and morphology of pure, (Gd, 2 wt% Fe) and (Gd, 4 wt% Fe) codoped SnO_2 nanopowders prepared through the coprecipitation route were analyzed with the TEM device, as shown in Figure 4. The TEM image of the powder of the pure SnO_2 sample contains fine spherical particles, with some particles having a large size (minor) and other having a small size (major), as seen in Figure 4a. The TEM images of (Gd, 2 wt% Fe) and (Gd, 4 wt% Fe) codoped SnO_2 nanopowders displayed the synthesis of similar distributed fine

spherical particles with nearly equal size, as shown in Figure 4b,c. The average particle size of the pure, (Gd, 2 wt% Fe) and (Gd, 4 wt% Fe) codoped SnO_2 nanopowders was estimated to be 14, 10 and 12 nm, respectively. These values are close to the values of the crystallite sizes based on XRD analysis. The presence of Gd/Fe ions during the preparation process seems to reduce the particle size and also enhance the uniformity of the SnO_2 particles.

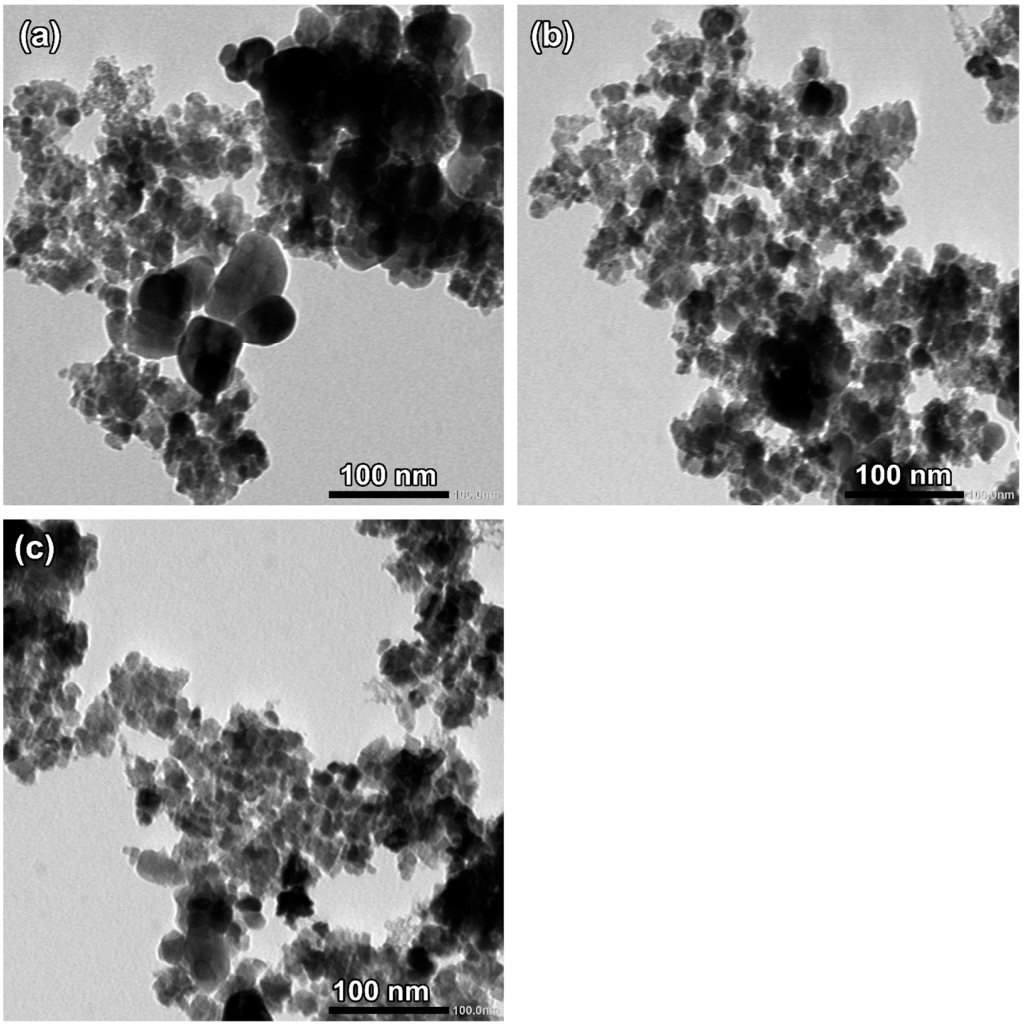

Figure 4. TEM images of (**a**) pure, (**b**) (Gd, 2% Fe) and (**c**) (Gd, 4% Fe) codoped SnO_2 nanocrystalline powders.

2.4. Band Gap Energy and Optical Properties

The light energy is used to activate the photocatalyst to produce charge carriers followed by the production of active species like superoxide or hydroxyl radicals, which break the organic substances (waste product) down into simple molecules. The precise choice of light source (UV or visible light) to stimulate the photodegradation reaction is mainly correlated to the band gap energy of the catalyst and its optical absorption features. The diffuse reflectance is used to explore the response of the synthesized catalysts to different wavelengths as well as to estimate their band gap energy. Figure 5 shows the diffuse reflectance curves of pure, (Gd, 2 wt% Fe) and (Gd, 4 wt% Fe) codoped SnO_2 nanopowders. In the visible light region, the reflectance curves of the (Gd, 2 wt% Fe) and (Gd, 4 wt% Fe) codoped SnO_2 samples have a lower intensity compared to pure SnO_2 nanopowder, which evidenced their wide absorption aptitude. To exactly estimate the band gap energy of nanocrystalline oxide materials, the reflectance data were changed into absorbance data by using the Kubelka–Munk (K-M) function symbolized as $F(R_\infty)$. The

absorption coefficient (α), scattering coefficient (S) and the $F(R_\infty)$ are connected together by the subsequent Formula (2) [39]:

$$F(R_\infty) = \frac{(1 - R_\infty)^2}{2R_\infty} = \frac{K}{S} \quad (2)$$

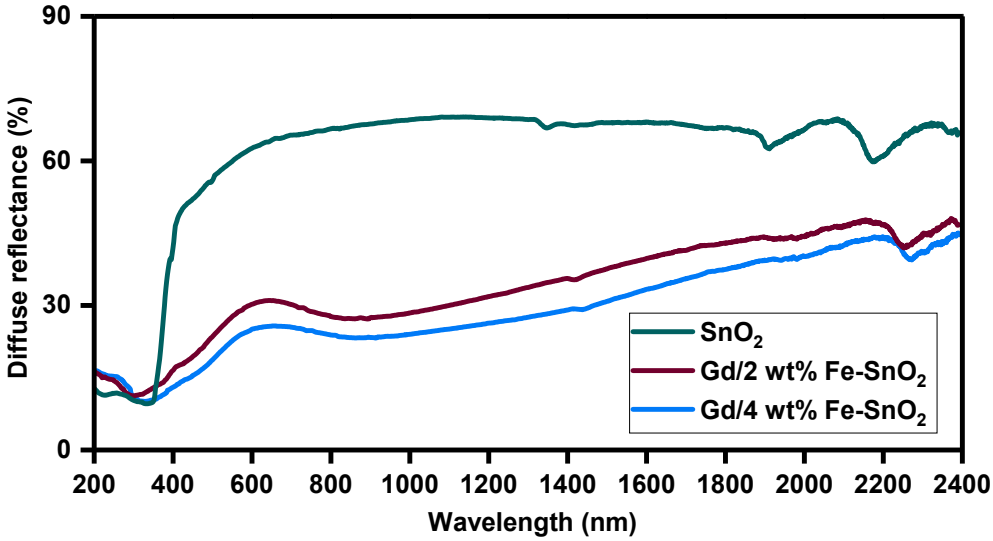

Figure 5. Diffuse reflectance of pure, (Gd, 2 wt% Fe) and (Gd, 4 wt% Fe) codoped SnO_2 nanocrystalline powders.

Since the SnO_2 semiconductor has a direct band gap energy, the formula relating the energy band gap (E_g) and absorption coefficient (α) can be represented as follows (3) [39]:

$$\alpha(h\nu) = A\left(h\nu - E_g\right)^{1/2} \quad (3)$$

where A is a constant, h is the plank constant and ν is the frequency of photon energy. As a result, the band gap energies of pure, (Gd, 2 wt% Fe) and (Gd, 4 wt% Fe) codoped SnO_2 nanopowders can be identified by plotting the change in the $[F(R_\infty)\, h\nu]^2$ opposed to the photon energy based on Equation (4) [39]:

$$[F(R_\infty)h\nu]^2 \propto \left(h\nu - E_g\right) \quad (4)$$

Through the $[F(R_\infty)h\nu]^2$ against $h\nu$ (eV) plots, the energy band gap (E_g) of pure, (Gd, 2 wt% Fe) and (Gd, 4 wt% Fe) codoped SnO_2 nanopowders was measured by extending the straight part of the curves to zero, as shown in Figure 6. For undoped SnO_2 nanopowder, the estimated E_g was detected to be 3.4 eV [40]. After the addition of (Gd, 2 wt% Fe) and (Gd, 4 wt% Fe) to the SnO_2 structure, the band gap energy was reduced to 2.88 and 2.82 eV, respectively. The narrowing of the band gap energy of SnO_2 nanopowders with the addition of Gd and Fe may be attributed to the sp–d/f exchange interaction between electrons of the band structure of SnO_2 and localized f or d electrons of Gd^{3+} and $Fe^{2+/3+}$ substituted Sn^{4+} sites. These interactions may result in the lowering of the conduction-band (CB) edge as well as the increase in the valence-band (VB) edge, causing in band gap energy thinning [41,42].

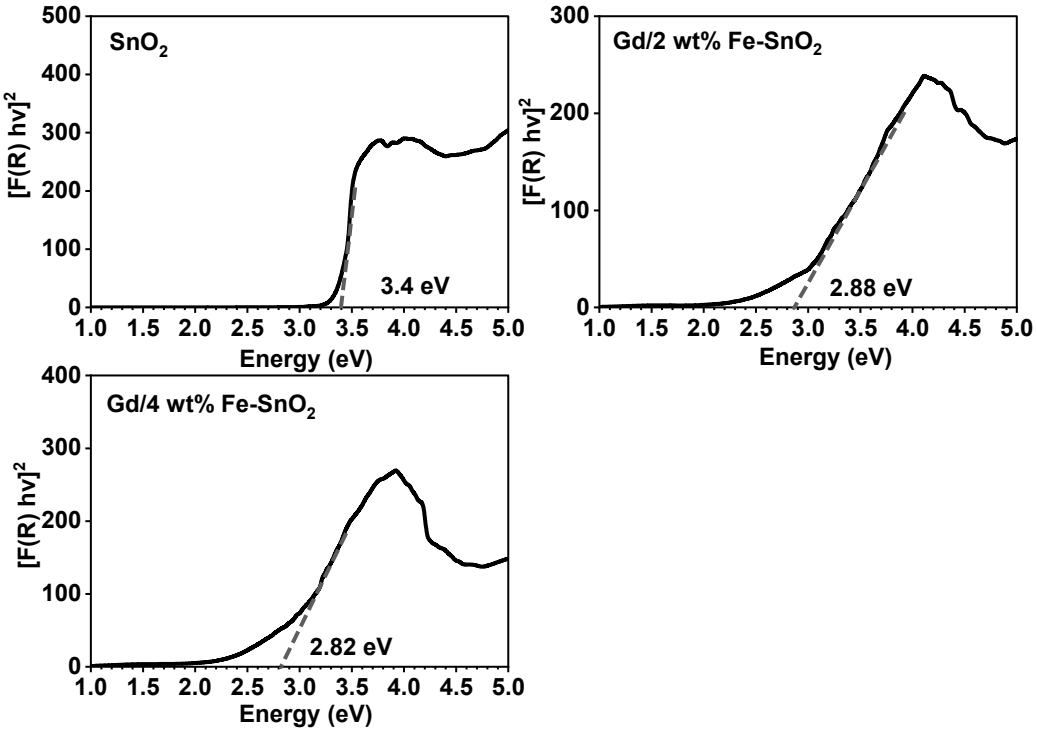

Figure 6. Optical band gap energy of pure, (Gd, 2 wt% Fe) and (Gd, 4 wt% Fe) codoped SnO_2 nanocrystalline powders.

2.5. Activity for Removal of Organic Pollutants

The function of pure, (Gd, 2 wt% Fe) and (Gd, 4 wt% Fe) codoped SnO_2 nanopowders as photocatalysts for wastewater treatment was tested for two pollutants involving Rose Bengal dye and methyl parathion pesticide. The solar energy was used as a free and available light source to activate the particles of the catalysts. The initial concentration of the Rose Bengal dye is 15 ppm (volume of solution = 110 mL, catalyst weight 0.06 g), while the concentration of the methyl parathion pesticide is 20 ppm (volume of solution = 110 mL, catalyst weight 0.06 g). Firstly, the photolysis test, namely the exposure of the pollutants to sunlight energy without the presence of catalysts, confirmed the high stability of Rose Bengal and methyl parathion pesticide with negligible self-degradation values. Figure 7a–c gives the variation in the initial absorbance curve of Rose Bengal solution after dark and irradiation treatment using pure, (Gd, 2 wt% Fe) and (Gd, 4 wt% Fe) codoped SnO_2 nanocatalysts. The absorbance curve of Rose Bengal was slightly changed after using the pure SnO_2 nanocatalyst with a measured adsorption value of 9% and a sunlight-induced degradation activity of 44% after 50 min. The codoping by (Gd, 2 wt% Fe) ions powerfully enhanced the function of the SnO_2 nanocatalyst for the removal of Rose Bengal dye with observed changes in the absorbance equivalent to a degradation efficiency of ~98% after 35 min. In the case of (Gd, 4 wt% Fe) ions, the reductions in the absorbance are equivalent to a degradation efficacy of ~86% after 35 min. The (Gd, 4 wt% Fe) codoped SnO_2 sample has a high activity compared to the pure sample, while it has a low activity compared to the (Gd, 2 wt% Fe) codoped SnO_2 sample. As a result, the use of 2 wt% Fe plus 2 wt% Gd is beneficial compared to 2wt Gd + 4 wt% Fe, owing to the increases in the carrier's concentration, which may assist the electron hole recombination. Moreover, the time of reaction was reduced to 35 min, achieving a best activity of nearly 100%. The low activity of the pure SnO_2 nanocatalyst can be assigned to the wide band energy as well as to a high recombination of charge carriers. The TEM images of the pure, (Gd, 2 wt% Fe) and (Gd, 4 wt% Fe) codoped SnO_2 nanopowders show a similar or close particle size for all samples. The optical properties based on diffuse reflectance analysis confirmed that (Gd, 2 wt% Fe) and (Gd, 4 wt% Fe) codoped SnO_2 nanopowders have visible light band gap

values in the range of 2.82–2.88 eV, while the pure SnO_2 sample has a UV band gap value of 3.4 eV. The Gd/Fe codoped SnO_2 catalysts have a wide absorption ability in the visible light spectrum (45% of sunlight energy), while the pure SnO_2 sample only has the ability to absorb within the UV region. Additionally, the insertion of Gd^{3+} and $Fe^{2+/3+}$ ions inside the SnO_2 structure supports the production of oxygen vacancies for charge balance with Sn^{4+} sites [43–45]. Furthermore, the Gd^{3+} and $Fe^{2+/3+}$ ions are expected to act as trapping centers to catch the excited electrons, which hinders the recombination of the charge carriers. All the discussed points, including the enhanced visible light absorption, production of oxygen vacancies and function of Gd^{3+} and $Fe^{2+/3+}$ ions as trapping centers, can be considered as the main factors which trigger the activity of the SnO_2 catalyst for the removal of Rose Bengal dye.

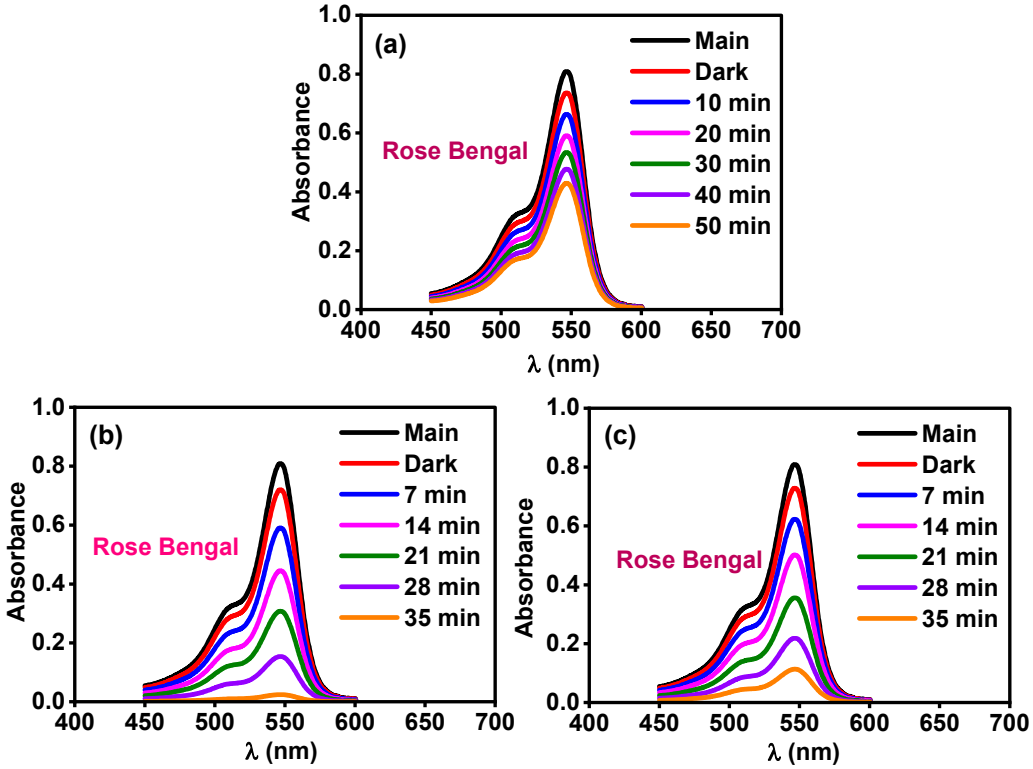

Figure 7. Change of absorbance spectrum of 15 ppm Rose Bengal dye for (**a**) pure, (**b**) (Gd, 2 wt% Fe) and (**c**) (Gd, 4 wt% Fe) codoped SnO_2 nanopowders under light irradiation.

For the kinetic study of Rose Bengal dye degradation, the plots of $\ln(C_0/C_t)$ opposed to time (min) are shown in Figure 8a,b for the three used catalysts. The fitting of the degradation data obeys the Langmuir–Hinshelwood model since the R-square values of the data lines are in the range of 0.93–0.98. The photodegradation rate constant of the (Gd, 2 wt% Fe) codoped SnO_2 catalyst is 0.06 min^{-1}, while that of the undoped and (Gd, 4 wt% Fe) codoped SnO_2 catalysts is 0.012 and 0.038 min^{-1}. To further investigate the photo-decomposition reaction, the mechanism for the photocatalytic process of Rose Bengal dye was analyzed. To inspect the key reactive charge carriers or species produced in the sunlight-activated photodegradation reaction of Rose Bengal dye using the (Gd, 2 wt% Fe) codoped SnO_2 catalyst, radical scavenging tests were performed with the addition of tetrachloromethane (CCl_4), ethyl alcohol (C_2H_5OH, EtOH), p-benzoquinone (p-BQ) and tert-butyl alcohol (*t*-BuOH) as quencher for electron (e^-), hole (h^+), superoxide ($O_2^{\bullet-}$) and hydroxyl (·OH) radicals, respectively [46,47]. As depicted in Figure 8c, the elimination rate of Rose Bengal dye was dropped from 98% (without scavenger) to 79% (EtOH), 69% (CCl_4), 58% (*t*-BuOH) and 44% (BQ) after the addition of these scavengers, respectively. Among these scavengers, BQ and t-BuOH substances display the maximum inhibition influence

for Rose Bengal dye degradation, demonstrating that $O_2^{\bullet-}$ and ·OH are the greatest vital reactive radicals during the photodegradation mechanism, and the electron and hole act as secondary reactive species.

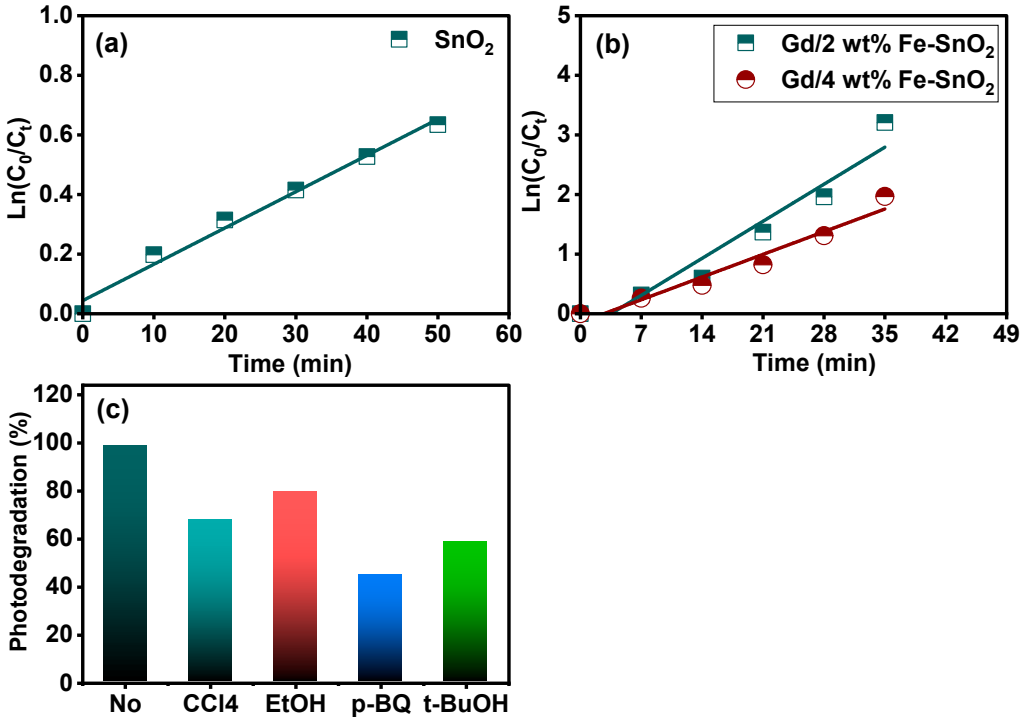

Figure 8. Plots of ln (C_0/Ct) vs. irradiation time (min) for Rose Bengal dye using (**a**) pure, (**b**) (Gd, 2 wt% Fe) and (Gd, 4 wt% Fe) codoped SnO_2 nanopowders while (**c**) scavengers test for Rose Bengal dye of (Gd, 2 wt% Fe) codoped nanocatalyst.

The grade of mineralization efficiency was evaluated for Rose Bengal dye degradation using the (Gd, 2 wt% Fe) codoped SnO_2 catalyst through the measurement of the total organic carbon (TOC) analysis. Figure 9a demonstrates the TOC removal percentage of Rose Bengal dye degradation to CO_2 and H_2O products, which reached to 95% after 42 min of sunlight irradiation. These results verify the decolorization and mineralization efficiency of the (Gd, 2 wt% Fe) codoped SnO_2 catalyst for the removal of Rose Bengal dye. The photocatalyst of the (Gd, 2 wt% Fe) codoped SnO_2 nanopowder was reused for three runs to degrade the Rose Bengal dye (15 ppm) under identical conditions, as used in the first degradation process and as seen in Figure 9b. The photocatalytic activity of the (Gd, 2 wt% Fe) codoped SnO_2 nanopowder was assessed to be 98, 92 and 88% for the removal of Rose Bengal dye, verifying the stability and the advantages of this catalyst for practical applications for many times.

The pesticides are another major family of organic pollutants present in wastewater and the efficient removal of these compounds is essential. Figure 10 depicts the effect of light energy on the absorbance curve of 20 ppm methyl parathion pesticide with the existence of pure, (Gd, 2 wt% Fe) and (Gd, 4 wt% Fe) codoped SnO_2 nanopowders. After 48 min of solar irradiation, the (Gd, 2 wt% Fe) codoped SnO_2 catalyst exhibits the greatest activity for the degradation of the methyl parathion pesticide with an efficiency of 96%. The pure and (Gd, 4 wt% Fe) codoped SnO_2 catalysts have a photocatalytic activity of 37% and 79% on the 20 ppm methyl parathion pesticide after 60 and 48 min, respectively. Thus, the (Gd, 2 wt% Fe) codoped SnO_2 catalyst has the ability to treat different organic pollutants with high efficiency and low time compared to the pure SnO_2 catalyst.

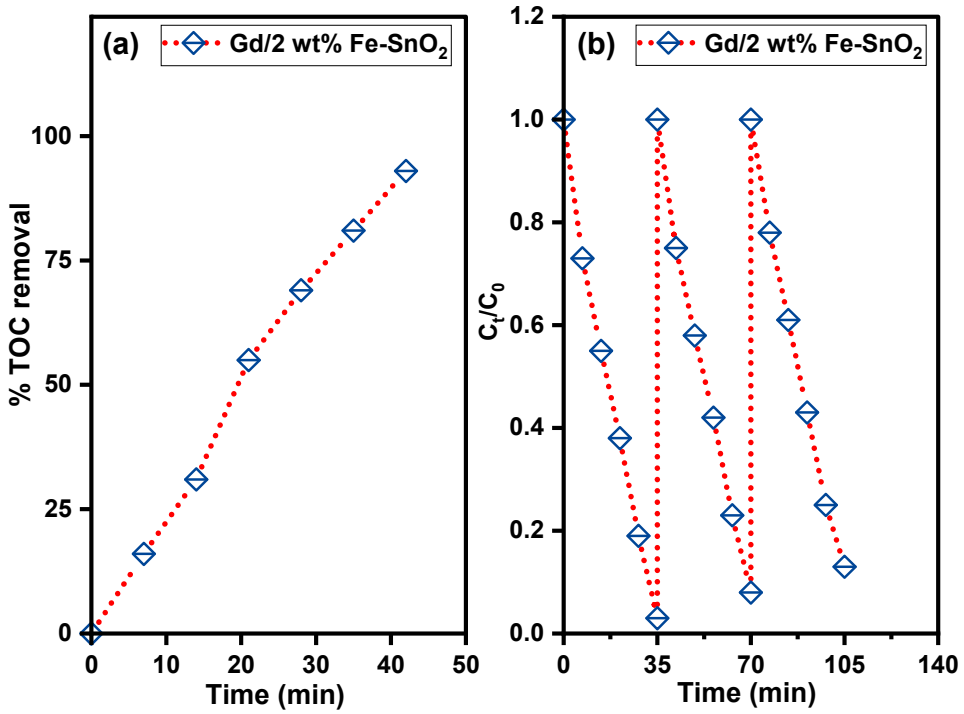

Figure 9. (**a**) Total organic carbon (TOC) removal percentage with time and (**b**) reusability results for Rose Bengal dye using (Gd, 2 wt% Fe) codoped nanocatalyst.

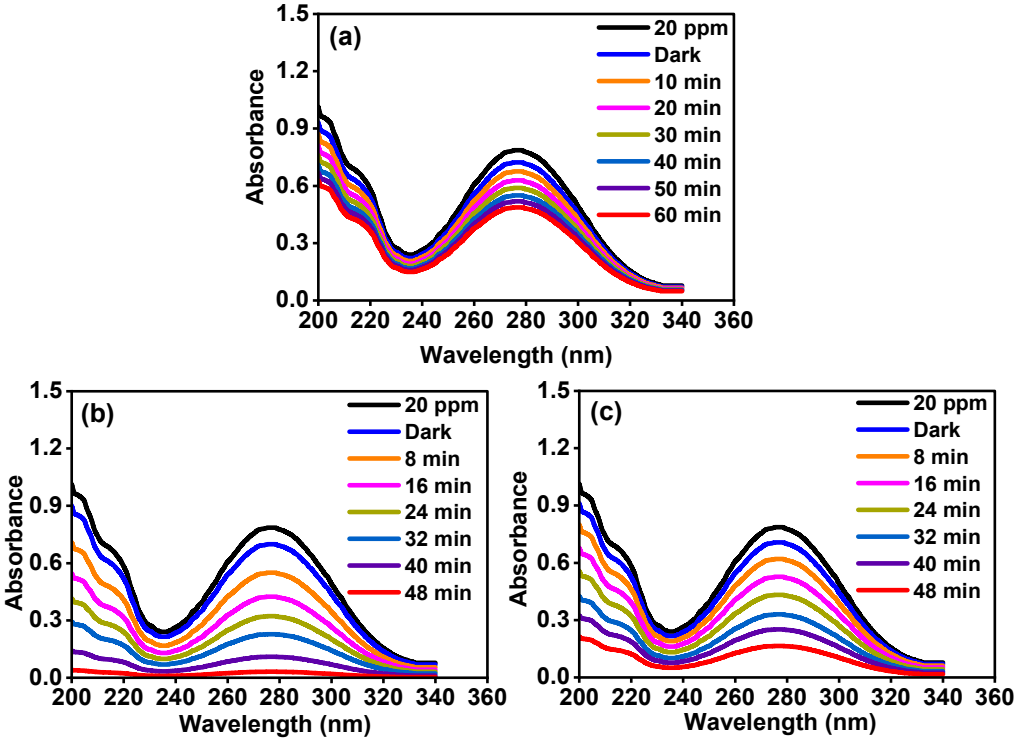

Figure 10. Change in absorbance spectrum of 20 ppm methyl parathion pesticide for (**a**) pure, (**b**) (Gd, 2 wt% Fe) and (**c**) (Gd, 4 wt% Fe) codoped SnO_2 nanopowders under sunlight irradiation.

As shown in Figure 11a, the reusability tests for the (Gd, 2 wt% Fe) codoped SnO_2 catalyst against methyl parathion pesticide for three cycles result in a photodegradation efficiency of 96, 92, 86%, respectively. The TOC removal percentage analysis of methyl parathion pesticide using the (Gd, 2 wt% Fe) codoped SnO_2 catalyst confirmed the high

mineralization properties, which reached to 94% after 56 min, as revealed in Figure 11b. The scavenger experiments or trapping tests were performed for methyl parathion pesticide degradation in the presence of the (Gd, 2 wt% Fe) codoped SnO_2 catalyst to analyze the reactive species in the photocatalytic process. Figure 11c gives the results of the trapping tests, which confirm that the $O_2^{\bullet-}$ and ·OH species are the highest reactive radicals during the photocatalytic mechanism followed by the electron and hole species. The impact of catalyst weight using (Gd, 2 wt% Fe) codoped SnO_2 nanopowder on the photodegradation efficiency of Rose Bengal dye and methyl parathion pesticide in the range from 0.02 to 0.08 g is shown in Figure 11d. By increasing the weight of the (Gd, 2 wt% Fe) codoped SnO_2 nanopowder from 0.02 to 0.06 g, the photodegradation efficiency was increased to reach the maximum value of 98 and 96% for Rose Bengal dye and methyl parathion pesticide, respectively. The improvements in the photodegradation efficiency can be attributed to the increases in the active sites by increasing the catalyst weight to 0.06 g. Moreover, the surface contact between pollutants and particles is expected to increase when increasing the catalyst weight. The further increases in the catalyst weight reduced the activity due to the extra particles, which can inhibit the penetration of sunlight. As shown in Figure 12, the main mechanism of the photodegradation of Rose Bengal dye and methyl parathion pesticide is mainly related to the excitation of the electron–hole pairs and the production of $O_2^{\bullet-}$ and ·OH radicals. At the moment of sunlight radiation, the electron–hole pairs are produced in the conduction band and valence band of (Gd, 2 wt% Fe) codoped SnO_2 particles, respectively. Consequently, the holes combine with the water molecules to give ·OH radicals, while the electrons combine with the oxygen molecules to yield the $O_2^{\bullet-}$ radicals. These formed radicals cause the decomposition of Rose Bengal dye and methyl parathion pesticide existing in the aqueous solution [27,48,49].

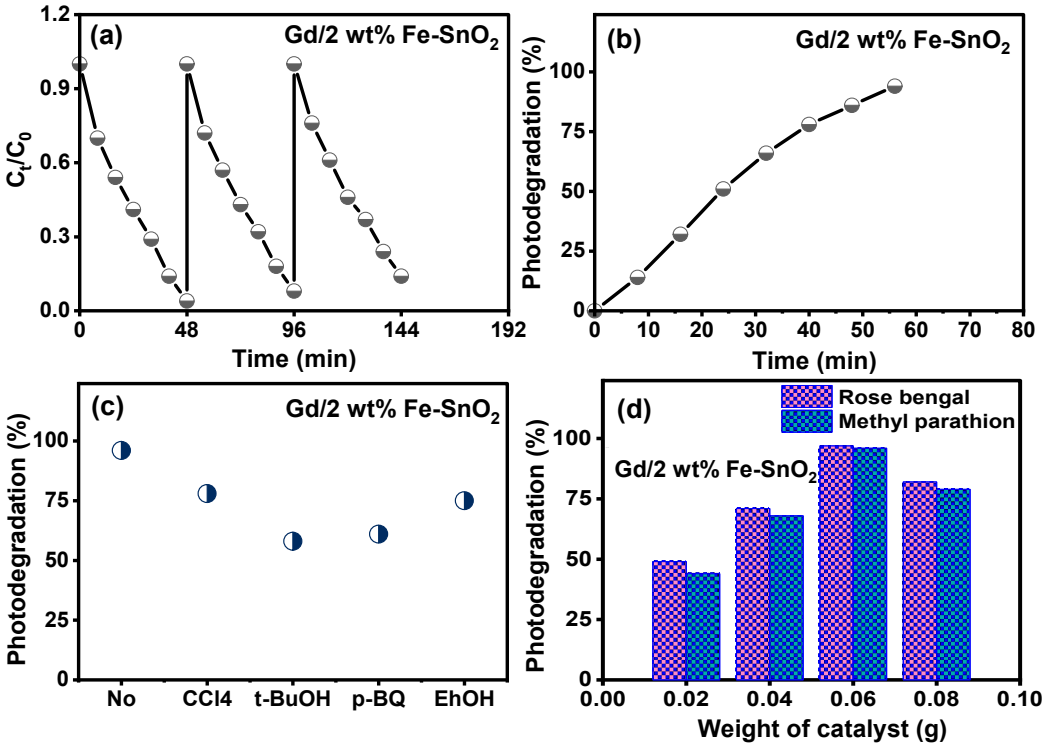

Figure 11. (**a**) Reusability results, (**b**) total organic carbon (TOC) removal percentage with time, (**c**) scavengers test for methyl parathion pesticide using (Gd, 2 wt% Fe) codoped nanocatalyst and finally (**d**) effect of catalyst weight of (Gd, 2 wt% Fe) codoped SnO_2 powder on the photocatalytic activity (%) of Rose Bengal and methyl parathion pesticide.

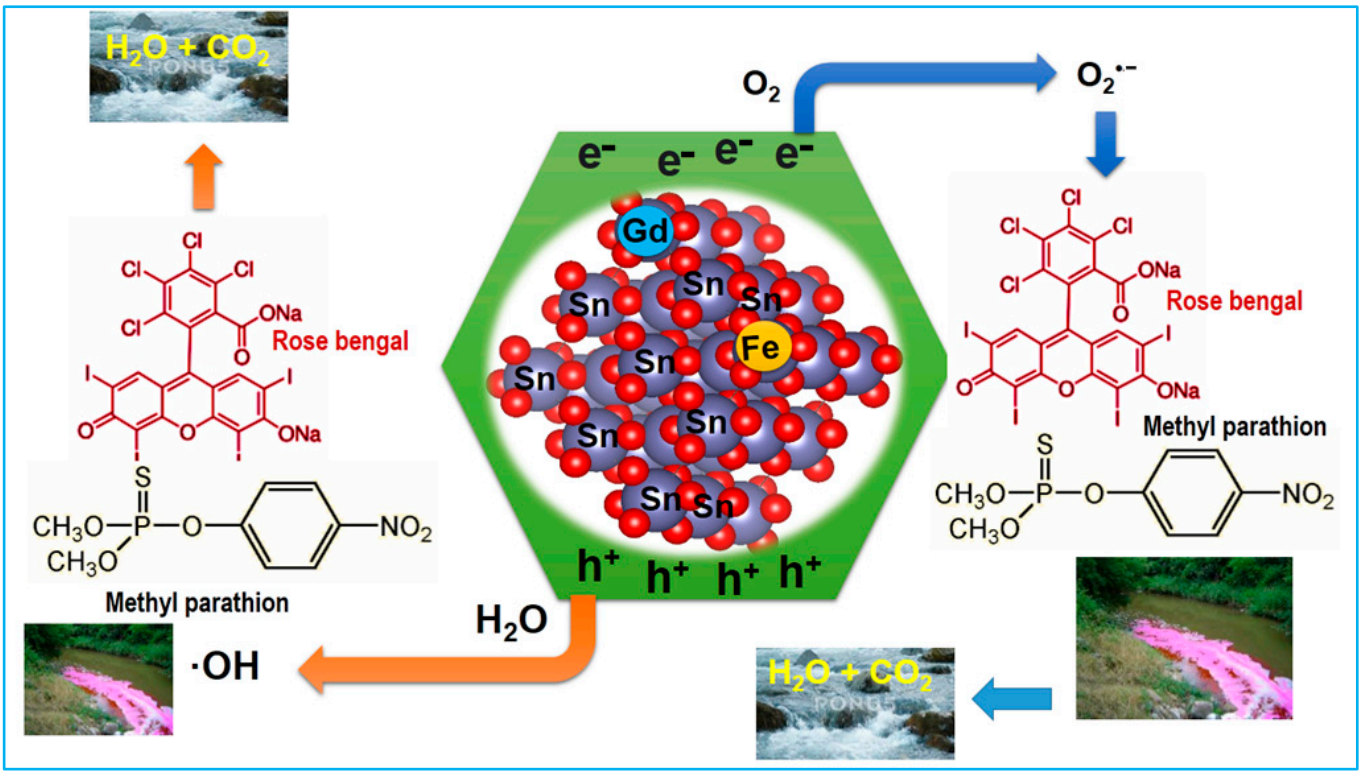

Figure 12. Illustration of the suggested photodegradation mechanism of $Sn_{0.96}Gd_{0.02}Fe_{0.02}O_2$ catalyst for Rose Bengal dye and methyl parathion pesticide under sunlight irradiation.

3. Materials and Methods

3.1. Preparation of Nanosized Undoped and Gd/Fe-SnO_2 Powders

The materials used to prepare the samples were $SnCl_4 \cdot 5H_2O$ (99%), $Gd(NO_3)_3 \cdot 6H_2O$ (99.9) and $Fe(NO_3)_3 \cdot 9H_2O$ (99.95) substances (Sigma-Aldrich, Darmstadt, Germany). Based on the coprecipitation procedure, three samples of the formulas SnO_2, $Sn_{0.96}Gd_{0.02}Fe_{0.02}O_2$ and $Sn_{0.94}Gd_{0.02}Fe_{0.04}O_2$ were prepared by dissolving suitable weights of $SnCl_4 \cdot 5H_2O$, $Gd(NO_3)_3 \cdot 6H_2O$ and $Fe(NO_3)_3 \cdot 9H_2O$ in different beakers containing 100 mL ethanol under continuous stirring at 25 °C. The exact weights of the used chemical substances to prepare the different samples are given in Table 1. The dissolved cations were converted into precipitates through the addition of NH_4OH (33%) solution until reaching a pH equal to 7.6. The removal of undesired dissolved ions (impurities like chloride ions) was realized by washing the precipitates with deionized water several times, as confirmed by the silver nitrate assessment for chloride ions. At a temperature of 650 °C for 3 h, the dried precipitates were calcined to form the final powders.

Table 1. Weights (gram) of chemical substances used to synthesize the different samples.

Composition	$SnCl_4 \cdot 5H_2O$ (g)	$Gd(NO_3)_3 \cdot 6H_2O$ (g)	$Fe(NO_3)_3 \cdot 9H_2O$ (g)
SnO_2	10.518	-	-
$Sn_{0.96}Gd_{0.02}Fe_{0.02}O_2$	10.097	0.27	0.24
$Sn_{0.94}Gd_{0.02}Fe_{0.04}O_2$	9.88	0.27	0.48

3.2. Physical Analysis and Photocatalytic Procedure

The characterizations of SnO_2, $Sn_{0.96}Gd_{0.02}Fe_{0.02}O_2$ and $Sn_{0.94}Gd_{0.02}Fe_{0.04}O_2$ powders were completed with an X-ray diffraction (XRD) instrument using Bruker D8 Advance (Rheinstetten, Germany) with an applied wavelength of radiation equal to 1.5406 Å. The optical properties of the prepared powders were studied with a diffuse reflectance spectroscopy (JASCO, V-570 UV-Vis-NIR, Tokyo, Japan) device. The integrating sphere unit

was used to measure the diffuse reflection with standard $BaSO_4$ material. High-resolution transmission electron microscopy (JEOL electron microscopy JEM-100 CX, TEM, Tokyo, Japan) was used to identify the particles' size and morphology. The Fourier transform infrared spectra (FTIR) were measured by PerkinElmer, Weinheim, Germany. Typically, 2 mg of each synthesized sample was mixed with 100 mg of pure potassium bromide. The obtained mixture was pressed in a dye to form pellets. The infrared measurements in the range of 4000–200 cm^{-1} were carried out using the PerkinElmer device.

The photocatalytic activity of SnO_2, $Sn_{0.96}Gd_{0.02}Fe_{0.02}O_2$ and $Sn_{0.94}Gd_{0.02}Fe_{0.04}O_2$ powders for the removal of 15 ppm rose Bengal and 20 ppm parathion methyl pesticide was examined using a catalyst weight of 60 mg (0.06 g) and a solution volume of 110 mL (total beaker volume, 2000 mL). Firstly, the mixture solution of the catalyst and the pollutant solution was stirred in the dark for 20 min to estimate the adsorption factor. After that, the mixture solution was exposed to direct sunlight energy (1–2 pm, September, Saudi Arabia) under constant stirring. At fixed times, 3 mL of the irradiated solution was withdrawn and the suspended catalyst was removed by centrifugation at 12,000 rpm for 10 min. Then, the absorbance of the solution was measured with a UV–Visible spectrophotometer (StellarNet, Tampa, FL, USA). The photodegradation efficiency was found from the relation, photodegradation (%) = $A_0 - A_t/A_0 \times 100$, where A_0 is the absorbance of the initial concentration of Rose Bengal dye and parathion methyl pesticide while A_t is the absorbance of irradiated solutions at fixed times.

4. Conclusions

In this study, new photocatalysts based on Gd/Fe-codoped SnO_2 with compositions of $Sn_{0.96}Gd_{0.02}Fe_{0.02}O_2$ and $Sn_{0.94}Gd_{0.02}Fe_{0.04}O_2$ were synthesized in a low-cost coprecipitation way. A pure tetragonal phase in the SnO_2 structure was detected for all samples with measured crystallite sizes in the range of 13–18 nm. The measured optical properties confirmed that the pure, (Gd, 2 wt% Fe) and (Gd, 4 wt% Fe) codoped SnO_2 structures have a band gap energy of 3.4, 2.88 and 2.82 eV, respectively. For environmental pollution treatment, the (Gd, 2 wt% Fe) codoped SnO_2 nanocatalyst revealed a perfect photocatalytic efficiency of 98 and 96% for the removal of Rose Bengal dye and methyl parathion pesticide after activation by sunlight for 35 and 48 min, respectively. Additionally, the (Gd, 2 wt% Fe) codoped SnO_2 nanocatalyst has shown a perfect mineralization value with also a high stability performance during the treatment of Rose Bengal dye and methyl parathion pesticide. The obtained optical and photocatalytic results suggest the appropriateness of the (Gd, 2 wt% Fe) codoped SnO_2 nanocatalyst for the treatment of agriculture and industrial effluent under activation by free light energy.

Author Contributions: All of the work was conducted by G.M.A. and S.A.A. All authors have read and agreed to the published version of the manuscript.

Funding: This research received no external funding.

Data Availability Statement: The datasets are available upon reasonable request.

Acknowledgments: The authors extend their appreciation to the Deanship of Scientific Research at King Faisal University for the logistic support of this work through Project No.(GrantA456).

Conflicts of Interest: The authors have no conflicts of interest.

References

1. Basha, B.; Manzoor, A.; Alrowaili, Z.A.; Ihsan, A.; Shakir, I.; Al-Buriahig, M.S. $Ba_{2-x}Ho_xSr_{2-y}NiyFe_{12}O_{22}$ and its composite with MXene: Synthesis, characterization and enhanced visible light mediated photocatalytic activity for colored dye and pesticide. *RSC Adv.* **2023**, *13*, 29944–29958. [CrossRef] [PubMed]
2. Naghizadeh, M.; Taher, M.A.; Tamaddon, A.M. Facile synthesis and characterization of magnetic nanocomposite $ZnO/CoFe_2O_4$ hetero-structure for rapid photocatalytic degradation of imidacloprid. *Heliyon* **2019**, *5*, e02870. [CrossRef] [PubMed]
3. Malini, B.; Gandhimathi, R. An overview of photocatalytic degradation of agricultural pollutants in water. *Int. J. Green Energy* **2024**, 1–15. [CrossRef]

4. Dihom, H.R.; Al-Shaibani, M.M.; Mohamed, R.M.S.R.; Al-Gheethi, A.A.; Sharma, A.; Khamidun, M.H.B. Photocatalytic degradation of disperse azo dyes in textile wastewater using green zinc oxide nanoparticles synthesized in plant extract: A critical review. *J. Water Process Eng.* **2022**, *47*, 102705. [CrossRef]
5. Kawsar, M.; Hossain, M.S.; Tabassum, S.; Bahadur, N.M.; Ahmed, S. Synthesis of different types of nanohydroxyapatites for efficient photocatalytic degradation of textile dye (Congo red): A crystallographic characterization. *RSC Adv.* **2024**, *14*, 11570–11583. [CrossRef] [PubMed]
6. Madkhali, N.; Prasad, C.; Malkappa, K.; Choi, H.Y.; Govinda, V.; Bahadur, I.; Abumousa, R.A. Recent update on photocatalytic degradation of pollutants in waste water using TiO_2-based heterostructured materials. *Results Eng.* **2023**, *17*, 100920. [CrossRef]
7. Natsathaporn, P.; Jenjob, R.; Pattanasattayavong, P.; Yiamsawas, D.; Crespy, D. Photocatalytic degradation of pesticides by nanofibrous membranes fabricated by colloid-electrospinning. *Nanotechnology* **2020**, *31*, 215603. [CrossRef]
8. Khan, K.A.; Shah, A.; Nisar, J. Electrochemical detection and removal of brilliant blue dye via photocatalytic degradation and adsorption using phyto-synthesized nanoparticles. *RSC Adv.* **2024**, *14*, 2504–2517. [CrossRef]
9. Yeganeh, M.; Charkhloo, E.; Sobhi, H.R.; Esrafili, A.; Gholami, M. Photocatalytic processes associated with degradation of pesticides in aqueous solutions: Systematic review and meta-analysis. *Chem. Eng. J.* **2022**, *428*, 130081. [CrossRef]
10. Mahmoodi, M.; Rafiee, E.; Eavani, S. Photocatalytic removal of toxic dyes, liquorice and tetracycline wastewaters by a mesoporous photocatalyst under irradiation of different lamps and sunlight. *J. Environ. Manag.* **2022**, *313*, 115023. [CrossRef]
11. Germani, R.; Mancinelli, M.; Roselli, A.; Tiecco, M.; Fantacci, S.; di Bona, S.; Giacco, T.D. Kinetic effects of cationic surfactants on the photocatalytic degradation of anionic dyes in aqueous TiO_2 dispersions. *New J. Chem.* **2023**, *47*, 392–401. [CrossRef]
12. Ramadevi, P.; Shanmugavadivu, R.; Venkatesan, R.; Mayandi, J.; Sagadevan, S. Photocatalytic dye degradation efficiency and reusability of aluminium substituted nickel ferrite nanostructures for wastewater remediation. *Inorg. Chem. Commun.* **2023**, *150*, 110532. [CrossRef]
13. Geldasa, F.T.; Kebede, M.A.; Shura, M.W.; Hone, F.G. Experimental and computational study of metal oxide nanoparticles for the photocatalytic degradation of organic pollutants: A review. *RSC Adv.* **2023**, *13*, 18404–18442. [CrossRef] [PubMed]
14. Roy, H.; Ur Rahman, T.; Md. Khan, A.J.R.; Al-Mamun, M.R.; Islam, S.Z.; Khaleque, M.A.; Hossain, M.I.; Khan, M.Z.H.; Islam, M.S.; Marwani, H.M.; et al. Toxic dye removal, remediation, and mechanism with doped SnO_2-based nanocomposite photocatalysts: A critical review. *J. Water Process Eng.* **2023**, *54*, 104069. [CrossRef]
15. Zieliński, B.; Miądlicki, P.; Przepiórski, J. Development of activated carbon for removal of pesticides from water: Case study. *Sci. Rep.* **2022**, *12*, 20869. [CrossRef]
16. Nyankson, E.; Kumar, R.V. Removal of water-soluble dyes and pharmaceutical wastes by combining the photocatalytic properties of Ag_3PO_4 with the adsorption properties of halloysite nanotubes. *Mater. Today Adv.* **2019**, *4*, 100025. [CrossRef]
17. Moghaddam, S.S.; Moghaddam, M.R.A.; Arami, M. Coagulation/flocculation process for dye removal using sludge from water treatment plant: Optimization through response surface methodology. *J. Hazard. Mater.* **2010**, *175*, 651–657. [CrossRef] [PubMed]
18. Fradj, A.B.; Boubakri, A.; Hafiane, A.; Hamouda, S.B. Removal of azoic dyes from aqueous solutions by chitosan enhanced ultrafiltration. *Results Chem.* **2020**, *2*, 100017. [CrossRef]
19. Dhananjay, P.; Abhilash, M.R.; Shilpa, N.; Hemanth, K.N.K.; Gowtham, H.G.; Aiyaz, M.; Brijesh, S.S.; Abdul, M.; Suhail, A.; Murali, M. Solar irradiation driven catalytic dye degradation by novel biosynthesized zinc oxide nanoparticles (ZnO–NPs) from *Barleria mysorensis*: Kinetics, reusability and mineralization studies. *J. Mol. Struct.* **2024**, *1303*, 137549.
20. Fatima, S.; Munawar, T.; Nadeem, M.S.; Mukhtar, F.; Khan, S.A.; Koc, M.; Iqbal, F. Boosted natural sunlight driven photodegradation of organic dyes using rGO anchored Pr/Cu dual-doped ZnO nanocomposite: Characterization and mechanistic insight. *Opt. Mater.* **2023**, *136*, 113397. [CrossRef]
21. Xu, J.; Shen, J.; Jiang, H.; Yu, X.; Qureshi, W.A.; Maouche, C.; Gao, J.; Yang, J.; Liu, Q. Progress and challenges in full spectrum photocatalysts: Mechanism and photocatalytic applications. *J. Ind. Eng. Chem.* **2023**, *119*, 112–129. [CrossRef]
22. Ullah, S.; Ferreira-Neto, E.P.; Hazra, C.; Parveen, R.; Rojas-Mantilla, H.D.; Calegaro, M.L.; Serge-Correales, Y.E.; Rodrigues-Filho, U.P.; Ribeiro, S.J.L. Broad spectrum photocatalytic system based on $BiVO_4$ and $NaYbF_4$:Tm^{3+} upconversion particles for environmental remediation under UV-vis-NIR illumination. *Appl. Catal. B Environ.* **2019**, *243*, 121–135. [CrossRef]
23. Chong, C.Y.; Sum, J.Y.; Lai, L.S.; Toh, P.Y.; Chang, Z.H. Visible light-driven dye degradation by magnetic cobalt-doped zinc oxide/iron oxide photocatalyst. *Next Mater.* **2024**, *2*, 100074. [CrossRef]
24. Sultana, M.; Mondal, A.; Islam, S.; Khatun, M.A.; Rahaman, M.H.; Chakraborty, A.K.; Rahman, M.S.; Rahman, M.M.; Nur, A.S.M. Strategic development of metal doped TiO_2 photocatalysts for enhanced dye degradation activity under UV–Vis irradiation: A review. *Curr. Res. Green Sustain. Chem.* **2023**, *7*, 100383. [CrossRef]
25. Matalkeh, M.; Nasrallah, G.K.; Shurrab, F.M.; Al-Absi, E.S.; Mohammed, W.; Elzatahry, A.; Saoud, K.M. Visible light photocatalytic activity of Ag/WO_3 nanoparticles and its antibacterial activity under ambient light and in the dark. *Results Eng.* **2022**, *13*, 100313. [CrossRef]
26. Sharma, A.; Kumar, N.; Diery, W.A.; Moujaes, E.A.; Mittal, A.; Singh, P.; Sharma, S. Co^{+2}, Ni^{+2}, Cu^{+2} doped Indium oxide as visible active nano-photocatalyst: A facile solution combustion synthesis, electronic band structure analysis by DFT approach and photocatalytic decontamination of RhB and Triclopyr. *J. Mol. Liq.* **2023**, *392*, 123508. [CrossRef]
27. Mezyen, M.; El Fidha, G.; Bitri, N.; Harrathi, F.; Ly, I.; Llobet, E. Visible light activated SnO_2:Dy thin films for the photocatalytic degradation of methylene blue. *RSC Adv.* **2023**, *13*, 31151–31166. [CrossRef]
28. Das, S.; Jayaraman, V. SnO_2: A comprehensive review on structures and gas sensors. *Prog. Mater. Sci.* **2014**, *66*, 112–255.

29. Kong, Y.; Li, Y.; Cui, X.; Su, L.; Ma, D.; Lai, T.; Yao, L.; Xiao, X.; Wang, Y. SnO_2 nanostructured materials used as gas sensors for the detection of hazardous and flammable gases: A review. *Nano Mater. Sci.* **2022**, *4*, 339–350. [CrossRef]
30. Chen, Y.; Meng, Q.; Zhang, L.; Han, C.; Gao, H.; Zhang, Y.; Yan, H. SnO_2-based electron transporting layer materials for perovskite solar cells: A review of recent progress. *J. Energy Chem.* **2019**, *35*, 144–167. [CrossRef]
31. Shabna, S.; Dhas, S.S.J.; Biju, C.S. Potential progress in SnO_2 nanostructures for enhancing photocatalytic degradation of organic pollutants. *Catal. Commun.* **2023**, *177*, 106642. [CrossRef]
32. Arif, M.; Shah, M.Z.U.; Ahmad, S.A.; Shah, M.S.; Ali, Z.; Ullah, A.; Idrees, M.; Zeb, J.; Song, P.; Huang, T.; et al. High photocatalytic performance of copper-doped SnO_2 nanoparticles in degradation of Rhodamine B dye. *Opt. Mater.* **2022**, *134*, 113135. [CrossRef]
33. Baig, A.A.B.; Rathinam, V.; Ramya, V. Synthesis and investigation of Fe doped SnO_2 nanoparticles for improved photocatalytic activity under visible light and antibacterial performances. *Mater. Technol.* **2020**, *36*, 623–635. [CrossRef]
34. Alam, U.; Khan, A.; Raza, W.; Khan, A.; Bahnemann, D.; Muneer, M. Highly efficient Y and V co-doped ZnO photocatalyst with enhanced dye sensitized visible light photocatalytic activity. *Catal. Today* **2017**, *284*, 169–178. [CrossRef]
35. Chen, Z.; Yu, S.; Liu, J.; Zhang, Y.; Wang, Y.; Yu, J.; Yuan, M.; Zhang, P.; Liu, W.; Zhang, J. C, F co-doping Ag/TiO_2 with visible light photocatalytic performance toward degrading Rhodamine B. *Environ. Res.* **2023**, *232*, 116311. [CrossRef] [PubMed]
36. Li, L.; Zhang, C.; Chen, W. Fabrication of SnO-SnO_2 nanocomposites with p-n heterojunctions for low-temperature sensing of NO_2 gas. *Nanoscale* **2015**, *7*, 12133–12142. [CrossRef] [PubMed]
37. Shaalan, N.M.; Hamad, D.; Abdel-Latief, A.Y.; Abdel-Rahim, M.A. Preparation of quantum size of tin oxide: Structural and physical characterization. *Prog. Nat. Sci. Mater. Int.* **2016**, *26*, 145–151. [CrossRef]
38. Chen, H.; Ding, L.; Sun, W.; Jiang, Q.; Hu, J.; Li, J. Synthesis and characterization of Ni doped SnO_2 microspheres with enhanced visible-light photocatalytic activity. *RSC Adv.* **2015**, *5*, 56401–56409. [CrossRef]
39. Raji, R.; Jyothi, G.; Sasidharan, S.; Gopchandran, K.G. White light-emitting ZnO:Dy^{3+} nanophosphors: Delving into the spectroscopic parameters via Judd–Ofelt analysis. *Dalton Trans.* **2024**, *53*, 6234–6244. [CrossRef]
40. Bannur, M.S.; Antony, A.; Maddani, K.I.; Poornesh, P.; Manjunatha, K.B.; Kulkarni, S.D.; Choudhari, K.S. Role of Ba in engineering band gap, photoluminescence and nonlinear optical properties of SnO_2 nanostructures for photovoltaic and photocatalytic applications. *Superlattices Microstruct.* **2018**, *122*, 156–164. [CrossRef]
41. Baig, A.B.A.; Rathinam, V.; Palaninathan, J. Facile synthesis of Ce-doped SnO_2 nanoparticles with enhanced performance for photocatalytic degradation of organic dye. *J. Iran. Chem. Soc.* **2021**, *18*, 13–27. [CrossRef]
42. Khatun, M.H.; Amin, R.; Sarker, M.S.I.; Shikder, M.R.; Islam, S.; Shahjahan, M. Structural and magnetic properties of Fe and Ni co-doped SnO_2 nanoparticles prepared by co-precipitation method. *Mater. Res. Express* **2024**, *11*, 016102. [CrossRef]
43. Zhao, X.; Wen, T.; Zhang, J.; Ye, J.; Ma, Z.; Yuan, H.; Ye, X.; Wang, Y. Fe-Doped SnO_2 catalysts with both BA and LA sites: Facile preparation and biomass carbohydrates conversion to methyl lactate MLA. *RSC Adv.* **2017**, *7*, 21678–21685. [CrossRef]
44. Singh, G.; Singh, R.C. Synthesis and characterization of Gd-doped SnO_2 nanostructures and their enhanced gas sensing properties. *Ceram. Int.* **2017**, *43*, 2350–2360. [CrossRef]
45. Fu, Y.; Sun, N.; Feng, L.; Wen, S.; An, Y.; Liu, J. Local structure and magnetic properties of Fe-doped SnO_2 films. *J. Alloys Compd.* **2017**, *698*, 863–867. [CrossRef]
46. Lin, X.; Chen, Y.; Zhou, D.; Chen, M.; Liang, W.; Guo, H. Aminated graphene quantum dots/CdS nanobelts for enhanced photocatalytic degradation of RhB dye under visible light. *RSC Adv.* **2024**, *14*, 255–265. [CrossRef] [PubMed]
47. Lua, X.-X.; Luo, Y.-H.; Liu, Y.-S.; Ma, W.-W.; Xu, Y.; Zhang, H. Assembly of three stable POM-based pillar-layer Cu^{I} coordination polymers with visible light driven photocatalytic properties. *CrystEngComm* **2016**, *18*, 3650–3654. [CrossRef]
48. Xiao, L.; Liao, R.; Yang, S.; Qiu, Y.; Wang, M.; Zhang, Z.; Du, J.; Xie, Z. Facile fabrication of F-doped SnO_2 nanomaterials for improved photocatalytic activity. *Coatings* **2022**, *12*, 795. [CrossRef]
49. Ahmad, S.; Almehmadi, M.; Janjuhah, H.T.; Kontakiotis, G.; Abdulaziz, O.; Saeed, K.; Ahmad, H.; Allahyani, M.; Aljuaid, A.; Alsaiari, A.A.; et al. The Effect of Mineral Ions Present in Tap Water on Photodegradation of Organic Pollutants: Future Perspectives. *Water* **2023**, *15*, 175. [CrossRef]